Inattentive Driving Behavior Detection Based on Portable FMCW Radar

Chuanwei Ding, *Student Member, IEEE*, Rachel Chae, *Student Member, IEEE*, Jing Wang, *Student Member, IEEE*, Li Zhang, *Student Member, IEEE*, Hong Hong, *Member, IEEE*, Xiaohua Zhu, *Member, IEEE*, and Changzhi Li, *Senior Member, IEEE*

***Abstract*— Monitoring driver's attentiveness is crucial for transportation safety. In this article, inattentive driving behavior detection based on frequency-modulated continuous-wave (FMCW) radar systems is proposed for this purpose. Seven typical driving behaviors which result in reduced attentiveness are involved in this study. Time-Doppler spectrogram and range-Doppler trajectory are utilized to analyze their features in multiple domains, including time, Doppler, range, and radar cross-section (RCS). These features are extracted as inputs to a machine learning classifier to obtain recognition results. Extensive experiments on a real car environment have been conducted to show its feasibility and superiority by obtaining an average accuracy rate of around 95%. The influences of radar center frequency, individual diversity, and radar view angle are also investigated.**

***Index Terms*— Driving behavior monitoring, frequency-modulated continuous-wave (FMCW) radar, machine learning, range-Doppler, time-Doppler.**

I. Introduction

DRIVING is an important component of modern society. It requires a set of activities, as well as situational awareness from the driver. Direct attention is required for quick and accurate decision making. More than 20% of crashes occurred due to inattentive driving [1]. Therefore, monitoring attention status is regarded as one of the most important approaches to transportation safety and autonomous driving, as there are various situations where the car needs to be informed how attentive the driver is and if it is possible to give back the control of the car to the driver [2].

Researchers have attempted various ways to achieve this purpose, including vehicle-based methods, physiology-based methods, and behavior-based methods. Vehicle-based methods estimate a driver's level of attentiveness by lane tracking, pedal usage, and erratic steering wheel movements [3]. However, they have inherent defects such as lack of direct relationship with the level of attentiveness. Physiology-based methods have been widely explored for drowsiness driving detection such as electroencephalography (EEG) [4], [5] for brain wave signal measurement, electrooculography (EOG) [6], [7] for eye blink detection, and electrocardiography (ECG) [8], [9] for heart rate variability (HRV) detection. These features are all aimed to determine the level of driving fatigue. However, during the above measurements, drivers are usually confined with attached sensors and electrodes, which are uncomfortable and could negatively affect the driver's behavior. On the other hand, existing noncontact physiological detection sensors, such as vision or radar technologies, are not reliable because of driver's extraneous movements [10]–[12]. In a real driving scenario, picking up objects or being distracted by nearby incidences should also be detected as they result in loss of attention. In behavior-based methods, vision systems are commonly used to monitor eye blinking, mouth state, and face/head motions [13]–[15]. In [13], visual changes in eye locations were investigated using the horizontal symmetry feature of eyes, and experimental results achieved 94% accuracy in eye blinking detection. Raman *et al.* [14] used a camera for driver fatigue detection by locating and tracking a driver's yawning. In [15], a vision system was proposed to compute head posture and gaze direction based on features extracted from the driver's facial images. However, cameras are vulnerable to lighting conditions, such as darkness and bright light from car lamps. Furthermore, it may infringe privacy issues.

The radar-based methods of behavior detection have attracted great interests worldwide for its potential of high accuracy, robustness, and privacy preservation [16]–[21]. For example, Ren *et al.* [16] proposed a new mathematical model based on micro-Doppler signatures to detect human walking

Manuscript received March 11, 2019; revised June 14, 2019; accepted July 31, 2019. Date of publication August 27, 2019; date of current version October 4, 2019. This work was supported in part by the National Science Foundation (NSF) under Grant ECCS-1808613 and Grant CNS-1718483, in part by the National Natural Science Foundation of China under Grant 61871224 and Grant 81601568, in part by the Key Research and Development Plan of Jiangsu Province under Grant BE2018729, in part by the Fundamental Research Funds for the Central Universities under Grant 30917011316, and in part by the State Scholarship Fund of China Scholarship Council under Grant 201806840055. This article is an expanded version from the IEEE MTT-S Radio and Wireless Week (Wireless Sensors and Sensor Networks), Orlando, FL, USA, January 20–23, 2019. *(Corresponding author: Hong Hong.)*

C. Ding is with the School of Electronic and Optical Engineering, Nanjing University of Science and Technology, Nanjing 210094, China, and also with the Department of Electrical and Computer Engineering, Texas Tech University, Lubbock, TX 79409 USA.

R. Chae is with the Woodbridge High School, Irvine, CA 92618 USA (e-mail: rachelchaetx@gmail.com).

J. Wang and C. Li are with the Department of Electrical and Computer Engineering, Texas Tech University, Lubbock, TX 79409 USA (e-mail: changzhi.li@ttu.edu).

L. Zhang, H. Hong, and X. Zhu are with the School of Electronic and Optical Engineering, Nanjing University of Science and Technology, Nanjing 210094, China (e-mail: hongnju@njust.edu.cn).

Color versions of one or more of the figures in this article are available online at http://ieeexplore.ieee.org.

Digital Object Identifier 10.1109/TMTT.2019.2934413

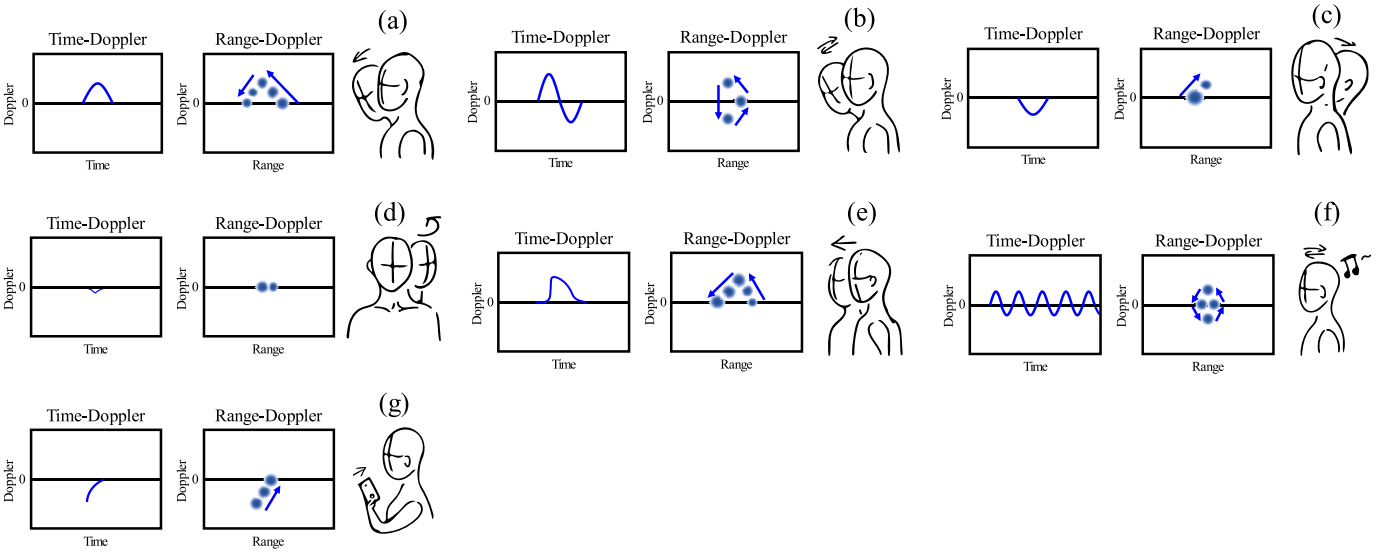

Fig. 1. Illustration of different driving behaviors and their predicted corresponding time-Doppler spectrogram and range-Doppler trajectory. (a)–(g) Seven typical driving behaviors related to inattentive driving.

strides using ultra-wideband (UWB) radar. In [17], a two-tone radar system was used to track hand gestures with concurrent detection of absolute distance and relative motion. In [18], a detection method was presented to remotely identify a potential active shooter with weapons based on radar micro-Doppler and range-Doppler signatures.

In this article, a frequency-modulated continuous-wave (FMCW) radar system is proposed for inattentive driving behavior detection and recognition in a real car environment. Compared with the preliminary work reported in [22], seven typical driving behaviors resulting in reduced attentiveness are studied, and machine learning-based solution is proposed to achieve automatic driving behavior recognition. A deep analysis of the behaviors' corresponding time-Doppler spectrogram and range-Doppler frames is presented. Extensive experiments are conducted with six volunteers in a real car environment. Furthermore, the performance of radar systems with different center frequencies (i.e., 24 and 5.8 GHz) is compared, and the optimal setup for inattentive driving behavior detection is discussed.

The rest of this article is organized as follows. Section II introduces the theory and algorithm of inattentive driving behavior detection based on the time-Doppler spectrogram and range-Doppler frames. In Section III, FMCW radar systems and experimental setup are introduced. Section IV presents the analysis and results of behavior recognition. Section V extends further discussions, and Section VI is the conclusion.

II. Theory and Algorithm

Seven typical driving behaviors related to inattentive driving are selected for recognition in this study, including dorsal flexion, dorsal hyperextension, sleepy, rotation, forward body motion, shaking head, and picking up a phone. An illustration of these driving behaviors is shown in Fig. 1, and the detailed description is given in Table I. The characteristic features are analyzed and extracted from micro-Doppler spectrogram to recognize these driving behaviors. The machine learning method is further adapted to obtain classification results.

TABLE I
Seven Driving Behaviors Under Study

No.	Motions	Description
(a)	Dorsal flexion	Bending down head forward at an angle.
(b)	Sleepy	Quick lifting head back up after the initial dorsal flexion.
(c)	Dorsal hyperextension	Lifting head backward at an angle.
(d)	Rotation	Rotating head around its axis.
(e)	Forward body	Moving head and upper body forward straightly.
(f)	Shaking head	Shaking/dancing with music.
(g)	Picking up a phone	Grabbing a phone and holding it in front of face

A. Analysis of Driving Behaviors

Fig. 1(a) illustrates the dorsal flexion of the subject's neck, where the subject's head tilts forward at an angle. This behavior involves the movement of the head toward the radar and is characterized by a positive Doppler signature and decreasing range. However, if the subject lifts the head back up after the initial dorsal flexion, the Doppler signature will suddenly change to negative and then increase before returning to zero [Fig. 1(b)]. Since sudden and quick dorsal flexion of the neck usually indicates a low level of driver alertness, it is important to distinguish dorsal flexion from other head and neck motions.

Fig. 1(d) illustrates the rotation of the subject's neck, where a subject's head rotates around its axis. As the rotation of the neck involves the relatively small movement of the head toward or away from the radar, it should not result in significant changes in either range- or Doppler-information.

Fig. 1(e) illustrates the forward body behavior by the subject, where the subject's head and upper body move forward without bending down at an angle. This movement should result in positive Doppler and decreasing range. Particularly, the detected power should keep increasing as the body and head approach the radar sensor.

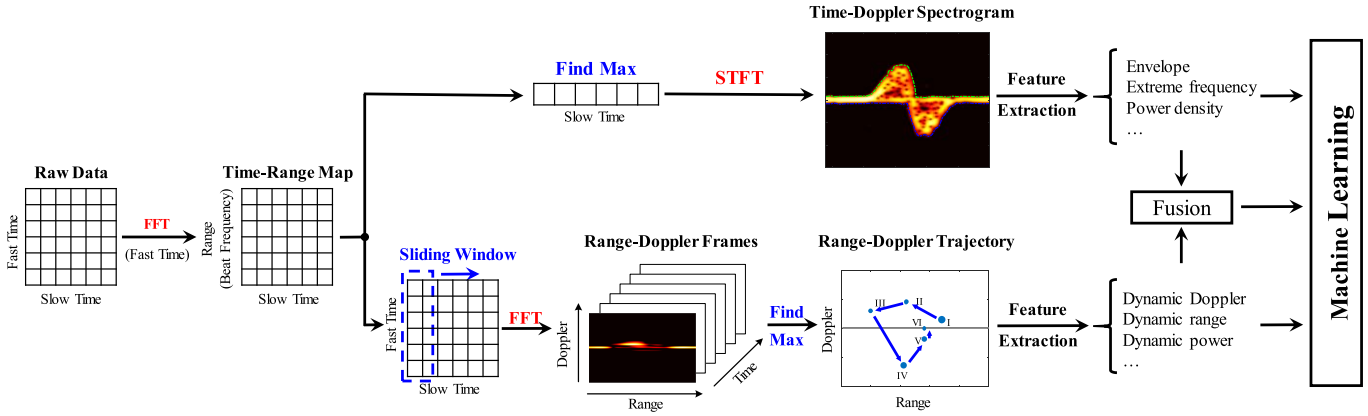

Fig. 2. Flowchart of the proposed processing method.

Fig. 1(f) illustrates shaking head behavior by the subject, where the subject's head shakes/dances with music. This behavior should lead to a sinusoidal-like wave both in the Doppler- and range-domains.

Fig. 1(g) illustrates the action of picking up a phone, where the subject grabs a phone and holds it in front of his/her face. Decreasing negative Doppler and increasing range will result from this motion. At the same time, although the driver's hand is moving away from the radar, it is also getting close to the beam center. However, the change in the detected power level would vary among persons with different body characteristics.

B. Spectrogram Processing and Feature Extraction

Fig. 2 shows the flowchart of the proposed signal processing algorithm. First, after preprocessing, which includes removing stationary clutter, the raw data is rearranged in a matrix according to the synchronization signals. Next, the range profile of the subject can be calculated by performing a fast Fourier transform (FFT) along the fast time of the raw signal. Then, the obtained signal can be stored in an $N \times M$ matrix $R(n, m)$ as a time-Range map, where $n = [1, 2, \ldots, N]$ indicates the index of slow time and $m = [1, 2, \ldots, M]$ indicates the index of the beat frequency corresponding to range bins. Based on this time-Range map, time-Doppler spectrogram and Range-Doppler trajectory can be obtained, respectively.

1) Time-Doppler Spectrogram: To obtain the time-Doppler spectrogram, the "range of focus" should first be determined. This can be designated as the range at which the maximum power was observed. Furthermore, to prevent interferences from hand movements around the steering wheel and other passengers in the backseats, the range of focus was limited by setting the minimum range of focus to 0.2 m and the maximum range of focus to 2 m. Then, the short-time Fourier transform (STFT) is performed on the signal in the range of focus to get the time-Doppler spectrogram as:

$$\mathrm{STFT}(p, \omega) = \sum_{n=0}^{N-1} R(n, m_f) w(n - p) e^{-j2\pi n\omega/N} \tag{1}$$

where $p = [1, 2, \ldots, P]$ and $\omega = [1, 2, \ldots, W]$ represent the time and Doppler index of the time-Doppler spectrogram, respectively, m_f is the index of the range of focus, and $w(p)$ is a window function.

Algorithm 1 Upper- and Lower-Envelope Detection

Input: $\mathrm{STFT}(p, \omega)$, $E(p)$, α
Output: F_{up}, F_{low}
for $p = 1$ to P **do**
  $E_{\mathrm{th}}(p) \leftarrow E(p) * \alpha$;
  for $\omega = 1$to W **do**
    $E(p, \omega) \leftarrow \mathrm{STFT}(p, \omega)^2$;
    if $E(p, \omega) \geq E_{\mathrm{th}}(p)$ **then**
      $\mathrm{index}_p(\omega) \longleftarrow \omega$
    end if
  end for
  $F_{\mathrm{up}}(p) \leftarrow \max(\mathrm{index}_p)$;
  $F_{\mathrm{low}}(p) \leftarrow \min(\mathrm{index}_p)$;
end for
return F_{up}, F_{low}

As shown in Fig. 3, based on the time-Doppler spectrogram, three types of features can be extracted as follows.

Envelope—F_{up}, F_{low} : This feature consists of the upper- and lower-envelopes of the time-Doppler spectrogram. First, the energy corresponding to the time index p is computed as

$$E(p) = \sum_{\omega}^{W} \mathrm{STFT}(p, \omega)^2, \quad p = 1, 2, \ldots, P. \tag{2}$$

Then, an energy-based threshold algorithm is established to calculate the upper- and lower-envelopes with a predetermined threshold α. For each time index p, the maximum of the Doppler indexes whose corresponding energies are greater than or equal to the predetermined threshold constitutes the upper-envelopes, while the minimum constitutes the lower-envelopes. The pseudocode of the proposed envelope detection is depicted in Algorithm 1. By considering the various phases of driving behaviors, 2-s time sequences of the upper- and lower-envelopes were extracted, respectively, which indicate dynamic Doppler changes for different driving behaviors.

Extreme Frequency—$f_{\max}$, $f_{\min}$: This feature contains the maximum and minimum frequencies, which are related to the

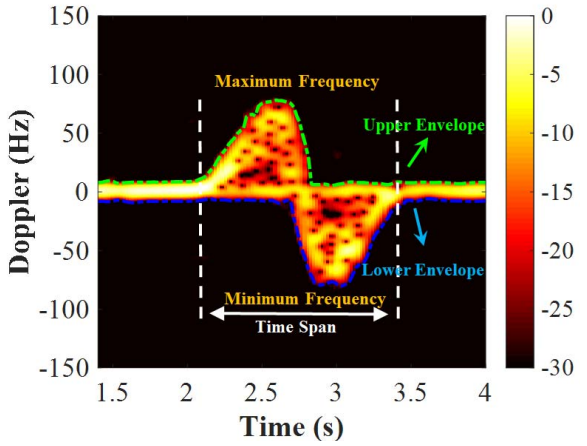

Fig. 3. Time-Doppler spectrogram of a sleepy behavior with the 24-GHz FMCW radar.

velocity of driving behaviors

$$f_{\max} = \max(\omega), \quad \omega \in F_{\text{up}} \tag{3}$$

$$f_{\min} = \min(\omega), \quad \omega \in F_{\text{low}}. \tag{4}$$

Power Density of the Effective Area—E_d : The area covered between the upper- and lower-envelopes except for the baseband (-10 to $+10$ Hz) is treated as the effective area. The power density of this area represents the intensity of driving behaviors, which is crucial for distinguishing between Doppler-similar behaviors

$$E_d = \frac{\sum_p \sum_{\omega=F_{\text{low}}(p)}^{F_{\text{up}}(p)} E(p,\omega)}{\sum_p \left(F_{\text{up}}(p) - F_{\text{low}}(p)\right)}. \tag{5}$$

2) Range-Doppler Trajectory: A dynamic range-Doppler trajectory method was proposed to analyze driving behaviors based on the range-Doppler domain. For obtaining a range-Doppler trajectory, FFT was performed on $R(n,m)$ along the slow time direction with a sliding time window. Then, a sequence of snapshots of driving behaviors in the range-Doppler domain can be acquired, which can be called range-Doppler frames. A single range-Doppler frame can be achieved as follows:

$$F_i(k,m) = \sum_{n=1}^{L} R(n,m) e^{-j2\pi nk/L} \tag{6}$$

where i represents the index of snapshots, k indicates the index of the frequency, and L is the length of the time window.

Fig. 4(a) shows six range-Doppler frames of a typical sleepy behavior (0.25-s time window with no overlapping). For obtaining the behavior trajectory based on range-Doppler frames, the baseband signal components close to 0 Hz are initially removed by an empirical Doppler threshold of 10 Hz. Next, the point with the maximum energy is extracted from each range-Doppler frame to construct a range-Doppler trajectory map with the following equation:

$$(k_i, m_i) = \arg\max_{(k,m)} E_i(k,m), \quad E_i(k,m) = F_i(k,m)^2 \tag{7}$$

where (k_i, m_i) represents the ith trajectory point extracted from the corresponding range-Doppler frame, and $E_i(k,m)$ indicates the energy of points in the ith frame.

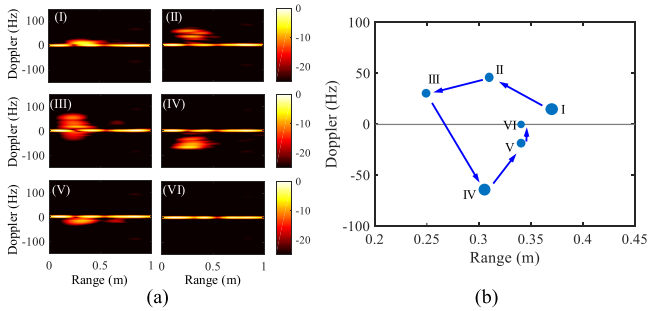

Fig. 4. Range-Doppler frames and trajectory of a sleepy behavior. (a) Six range-Doppler frames. (b) Corresponding range-Doppler trajectory.

As shown in Fig. 4(b), the blue dots indicate the extracted trajectory points, whose coordinate values represent range and Doppler, respectively. Their sizes correspond to the power level related to the radar cross-section (RCS) information. Then, three types of features can be extracted as follows:

Dynamic Doppler Frequency—D : This feature consists of a time sequence of the Doppler values along the trajectory. It represents the time-varying intensity of driving behaviors

$$D(i) = k_i. \tag{8}$$

Dynamic Range Change–ΔR : Range information is crucial for driving behavior recognition. The x-coordinate of each trajectory point represents the range of driving behaviors. Furthermore, for situations of different detection distances, it is adjusted as a time sequence of relative range change. This feature describes the relative range change for each driving behavior, and to some degree, indicates motion velocity and range span

$$\Delta R(i) = m_{i+1} - m_i, \quad i \in [1, I-1]. \tag{9}$$

Dynamic Power Change—ΔE : Considering the effects of different distances, this feature is based on the time-dependent power change. It indicates the time-varying RCS, which is important to discriminate motions that are similar in range and Doppler, e.g., dorsal flexion and forward body motion

$$\Delta E(i) = E_{i+1} - E_i, \quad i \in [1, I-1] \tag{10}$$

where E_i represents the energy of the ith trajectory point.

C. Machine Learning

Twelve machine learning classifiers were selected based on their popularity, diversity, and capabilities. These classifiers can be divided into four categories: decision tree, support vector machine (SVM), k-nearest neighbor (KNN), and ensemble learning. Models with a mature theoretical foundation like the decision tree and SVM are used in our experiment. The KNN is chosen since its probabilistic models are built, and they are frequently applied in biomedical signal processing [23]. In addition, the ensemble classifiers, which belong to a recent popular category, are explored comprehensively.

1) *Decision Tree:* Decision tree learning is one of the predictive modeling approaches used in statistics, data mining, and machine learning [24]. In a tree structure,

each branch indicates a possible decision, outcome or reaction. The farthest branches, i.e., leaves on the tree represent the final results or labels. The decision tree is commonly used in classification, as it is not sensitive to outliers and missing values.

2) *Support Vector Machine (SVM):* SVM is a supervised learning model with an associated learning algorithm that analyzes data for classification and regression analysis [25]. It outputs a hyperplane or set of hyperplanes in a high- or infinite-dimensional space for classification. An SVM model is a representation of the examples as points in space, mapped so that the examples of the separate categories are divided by a clear gap that is as wide as possible. New examples are then mapped into the same space and predicted to a category based on which side of the gap they fall into. In SVM, a regularization parameter can be set to reduce the risk of overfitting, and it is defined by a convex optimization problem, which means there are efficient methods without local minima.
3) *K-Nearest Neighbor (KNN):* KNN is a nonparametric method used for classification and regression [26]. It is an approach to data classification that estimates how likely a data point is to be a member of one category or the other according to what category the data points nearest to it are in. KNN is a "lazy learner" algorithm because it does not generate a model of the data set beforehand. The only calculation it makes is when it is asked to poll the data point's neighbors. This makes KNN appropriate for dealing with the multiclass problem.
4) *Ensemble Learning:* Ensemble methods use multiple learning algorithms to obtain better classification performance than a single one [27]. Unlike a statistical ensemble in a statistical mechanism, which is usually infinite, a machine learning ensemble refers only to a concrete finite set of alternative models but typically allows for much more flexible structure to exist among those alternatives. Ensemble learning tends to obtain better results when there is significant diversity among the models. In our experiments, bagged trees [28], boosted trees [29], and subspace KNN [30] were selected as the ensemble algorithms.

All classifiers are based on the Classification Learner Tool in MATLAB R2016b. Detailed parameters with default values are listed in Table II. For providing an unbiased evaluation, ten-fold cross-validation (CV) procedure was used in classification [31]. Specifically, all samples were divided into ten subsets containing recordings as equal as possible. During each iteration of the tenfold CV, nine subsets were used to train the classifier, and the remaining subset was used for validation. The classification results were obtained on each test data of the CV. After that, the evaluation of the classification's performance was formed by averaging all results.

TABLE II
PARAMETERS OF DIFFERENT CLASSIFIERS

Classifiers	Parameters
Decision Trees	Maximum number of splits: 20, 100. Split criterion: Ginis diversity index. Surrogate decision splits: Off. Maximum surrogates per node: 10.
SVM	Kernel function: Linear, Quadratic, Cubic, Gaussian. Box constraint level: 1. Kernel scale mode: Auto, Manual. Manual kernel scale: 1, 26. Multicalss method: One-vs-One.
KNN	Number of neighbors: 10, 100. Distance metric: Cosine, Minkowski (cubic). Distance weight: Equal, Squared inverse.
Ensemble	Ensemble method: AdaBoost, Bag, Subspace. Learner type: Decision tree, Nearest neighbors. Maximum number of splits: 20; Number of learners: 30. Learning rate: 0.1; Subspace dimension: 1, 22.

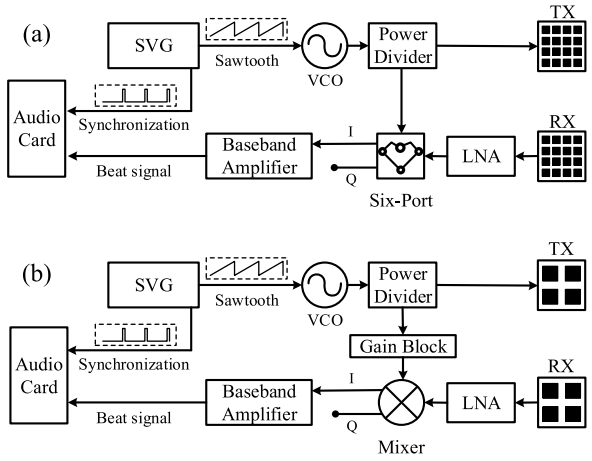

Fig. 5. Block diagrams of (a) 24-GHz and (b) 5.8-GHz FMCW radar systems.

III. EXPERIMENTAL SETUP

Two custom-designed FMCW radar systems with different center frequencies were used in this study [32], [33]. Their block diagrams are illustrated in Fig. 5. The 24-GHz radar consists of a flexible radio frequency (RF) board and a rigid baseband board. The RF board was built on a flexible substrate, including a pair of 4 × 4 patch antenna arrays, a voltage-controlled oscillator (VCO), a pair of low noise amplifiers (LNA), and a six-port structure [34]. The VCO and LNAs are off-the-shelf components. The six-port structure works as a quadrature mixer, which converts the RF signal to zero-IF baseband. The rigid baseband board has baseband amplifiers, as well as an on-board sawtooth voltage generator (SVG). In the transmitting part, the SVG generates a 960-Hz sawtooth voltage signal to control a free-running VCO to obtain a 700-MHz bandwidth frequency ramp with a center frequency of 24 GHz. After a power divider, the signal is transmitted through the antenna. In the receiving part, after the LNA, the RF signal is down-converted to the baseband with a six-port structure. Then, the beat signal can be obtained through an operational amplifier. A reference pulse sequence is generated at the same time with the sawtooth voltage to maintain coherence. A data acquisition interface is employed to simultaneously sample the reference sequence and the beat signal through the audio card of a laptop, facilitating

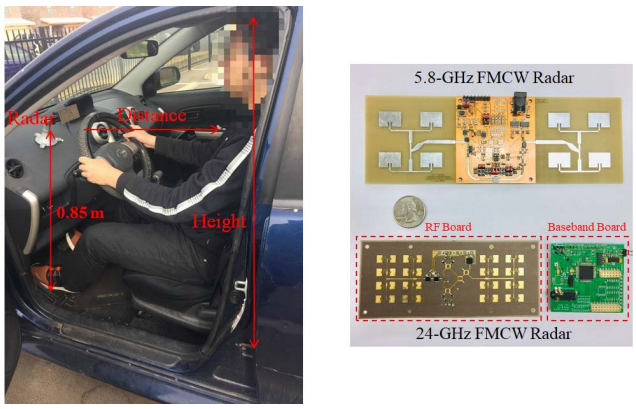

Fig. 6. Experimental setup and the two FMCW radar systems.

TABLE III
KEY PARAMETERS OF THE FMCW RADAR SYSTEM

Parameters \ Radar Type	1	2
Center frequency	24 GHz	5.8 GHz
Transmitted bandwidth	700 MHz	320 MHz
Sampling frequency	192 KHz	192 KHz
Frequency ramp repetition period	1ms	10 ms
Average transmitted power	8 dBm	8 dBm
Beamwidth	E-plane: 16.5 deg H-plane: 18.3 deg	E-plane: 40.3 deg H-plane: 44.4 deg

TABLE IV
KEY COMPONENTS USED IN RADAR SYSTEMS

System	Part	Part Number	Manufactory
24 GHz	VCO	HMC739LP4E	Analog Devices
	Power Divider	90° Quadrature Hybrid	Custom
	LNA	XL1010-QT-OGOT	Macom
	Six-port	SMS7621 Schottky Diodes	Skyworks
	Baseband Amplifier	ADA4581	Analog Devices
5.8 GHz	VCO	HMC358MS8G	Analog Devices
	Power Divider	GP2X1	Mini-Ciruits
	LNA	HMC320MS8G	Analog Devices
	Gain Block	NBB 400	Qorvo
	Mixer	HMC525LC4	Analog Devices
	Baseband Amplifier	ADA4581	Analog Devices

TABLE V
BRIEF PHYSICAL DESCRIPTION OF THE VOLUNTEERS

Volunteers	Gender	Age (yr)	Weight (kg)	Height (m)	BMI (kg/m^2)
1	F	26	50	1.57	20.28
2	M	29	86	1.74	28.41
3	M	27	75	1.72	25.35
4	M	26	100	1.89	27.99
5	M	29	78	1.80	24.07
6	M	24	68	1.78	21.42

real-time demodulation. During the signal processing, the phase of the baseband signal is aligned according to the pulse edge of the reference sequence, and thus, coherence is achieved.

As shown in Fig. 5(b), the architecture of the 5.8-GHz radar is similar to that of the 24-GHz radar. Different from the 4 × 4 patch antenna arrays in the 24-GHz system, a pair of 2 × 2 patch antenna arrays is used to transmit and receive signals for the 5.8-GHz device. This causes a wider beamwidth, which can cover a larger area but involves more noise. In addition, the 24-GHz device uses a six-port structure to down-convert the RF signal to the baseband, whereas the 5.8-GHz system uses a commercial quadrature mixer chip. Their key parameters, part numbers, and manufacturers are listed in Tables III and IV.

The experimental setup is illustrated in Fig. 6. The radar system was set behind the steering wheel with a height of 0.85 m from the floor. Six volunteers, including five males and one female, were involved. Their brief physical descriptions are listed in Table V. During measurements, each volunteer was required to adjust the seat to their most comfortable positions. Consequently, the distance between the radar and the subject ranged from 0.4 to 0.8 m, while the height of their heads ranged from 0.9 to 1.2 m. Six volunteers performed each behavior for 15 times, 5 of which were measured in a parked car, while the others were recorded in a moving car with speed ranging from 16.1 to 64.4 km/h. For safety consideration, measurements in a moving car were conducted in the passenger seat with the same experimental setup. As a result, a total of 630 measurements were recorded.

IV. RESULTS

In this section, the measurement results are first analyzed for different carrier frequencies. Then the classification performance based on the time-Doppler spectrogram and range-Doppler trajectory is compared.

A. 5.8-GHz Versus 24-GHz Carrier Frequency

Fig. 7 shows the time-Doppler spectrogram, range-Doppler frames, and trajectory of sleepy behavior with the 5.8-GHz FMCW radar system. Compared to the time-Doppler spectrogram obtained by the 24-GHz system in Fig. 3, the one with the 5.8-GHz system shows negative Doppler components during dorsal flexion, while positive Doppler parts appear when the subject lifts his/her head back up. This is reasonable as the wider beamwidth brings more noise and the narrower bandwidth of the 5.8-GHz system results in worse range resolution, which causes Doppler leakage in its spectrogram. In addition, as shown in Fig. 7(b), the poor range resolution also leads to wider main lobes in the range-Doppler frames than the ones in Fig. 4(a). This makes it difficult to track the driver's behaviors, which even resulted in unreliable range tracking of the second trajectory point, as shown in Fig. 7(c). Therefore, the 24-GHz FMCW radar system was adopted in the following measurements.

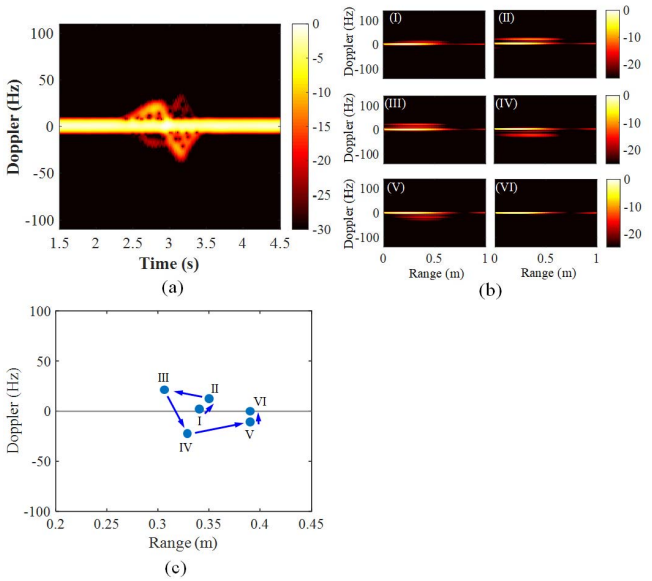

Fig. 7. Time-Doppler spectrogram, range-Doppler frames, and trajectory of a sleepy behavior detected by the 5.8-GHz FMCW radar. (a) Time-Doppler spectrogram. (b) Range-Doppler frames. (c) Range-Doppler trajectory.

Fig. 8 shows the time-Doppler spectrogram and range-Doppler trajectory (0.25-s time window with half overlapping) of seven driving behaviors with the 24-GHz FMCW radar system.

As shown in Fig. 8(a), as the subject's head bent toward the radar, the time-Doppler spectrogram displayed positive Doppler. Then, it returned to zero when the subject did not raise his/her head again. The range-Doppler trajectory also displayed positive Doppler and decreasing range during dorsal flexion, and the Doppler signature faded in the end.

However, when the subject lifted his/her head back up again after dorsal flexion, the Doppler signature changed to negative before returning to zero [Fig. 8(b)]. Likewise, both the Doppler and range signatures in the range-Doppler trajectory increased again after the initial decline.

The time-Doppler spectrogram and range-Doppler trajectory imaging in Fig. 8(c) correspond to the dorsal hyperextension of the neck. In a real car environment, the subject's head always bumped into the seat cushion after dorsal hyperextension. As a result, there were positive Doppler parts identified at the end of this behavior in the time-Doppler spectrogram.

Fig. 8(d) shows the time-Doppler spectrogram and range-Doppler trajectory of the lateral neck rotation. Since the left and right rotations result in identical Doppler and range signatures, only the right lateral rotation was recorded. Besides the predicted negative Doppler, a few positive Doppler components were observed at the same time. The reason is that during the rotation of the neck, one side of the face is turning far away from the radar, while the other side is turning closer to the radar. The upper- and lower-envelope extracted from time-Doppler spectrogram can indicate this characteristic. However, it is hard for the range-Doppler trajectory map to describe the positive Doppler components, as only one trajectory point is extracted from one range-Doppler frame.

Fig. 8(e) illustrates forward body behavior by the volunteer, where the subject moves both the head and body forward without bending down at an angle. In the time-Doppler spectrogram, the envelope of forward body behavior was similar to that of dorsal flexion. However, there were fewer scatters between the upper- and lower-envelope. This is because the scatters of the head and body exhibited the same velocity (i.e., Doppler frequency) without bending down at an angle. Furthermore, forward body behavior was also characterized by increasing power when approaching the radar, which can be observed from the time-Doppler spectrogram and range-Doppler trajectory.

As shown in Fig. 8(f), head shaking/dancing with music displayed periodic features both in the time-Doppler spectrogram and the range-Doppler trajectory, which is consistent with predictions detailed in Section II.

Fig. 8(g) shows the time-Doppler spectrogram and range-Doppler trajectory of picking up a phone. Note that the detected power kept increasing before the corresponding Doppler returned to zero. This demonstrates that, in this case, getting close to the beam center has a larger impact on power than moving away from the radar.

B. Selection of Machine Learning Classifier

Twelve classifiers were compared to find the most appropriate one for driving behavior detection. As shown in Fig. 9, red bars represent the recognition accuracy with time-Doppler spectrogram features, while blue ones indicate the corresponding accuracy with range-Doppler trajectory features. It is obvious that among all the selected classifiers, Bagged Trees obtained the highest level of accuracy for both time-Doppler and range-Doppler features. It is reasonable that individual diversity brings different characteristics to even the same driving behaviors, which leads to variance in features. The Bagged Trees is proposed to reduce the variance of a simple decision tree classifier. It creates several subsets of data from the training sample randomly chosen with replacement. Then, each collection of subset data is used to train their decision trees, which results in an ensemble of different models. The average of all the predictions from different trees is used to achieve a more robust classification than a single decision tree.

C. Classification Based on Time-Doppler Spectrogram

Based on the time-Doppler spectrogram, classification of seven driving behaviors achieved an average accuracy rate of 94.8%. The detailed confusion matrix is shown in Table VI. Note that (b) sleepy and (e) forward body behavior obtained the highest level of classification accuracy of 97.8%. Owing to the power density feature, only two samples of (a) dorsal flexion were recognized as (e) forward body behavior although they are similar in the time-Doppler domain. On the other hand, (c) dorsal hyperextension behavior had the lowest accuracy of 90%. This behavior could be easily confused with (d) rotation, as low amplitude dorsal hyperextension is similar to rotation in the time-Doppler domain. There also existed confusion among (a) dorsal flexion, (b) sleepy, and (f) shaking head caused by different shaking amplitudes and periods.

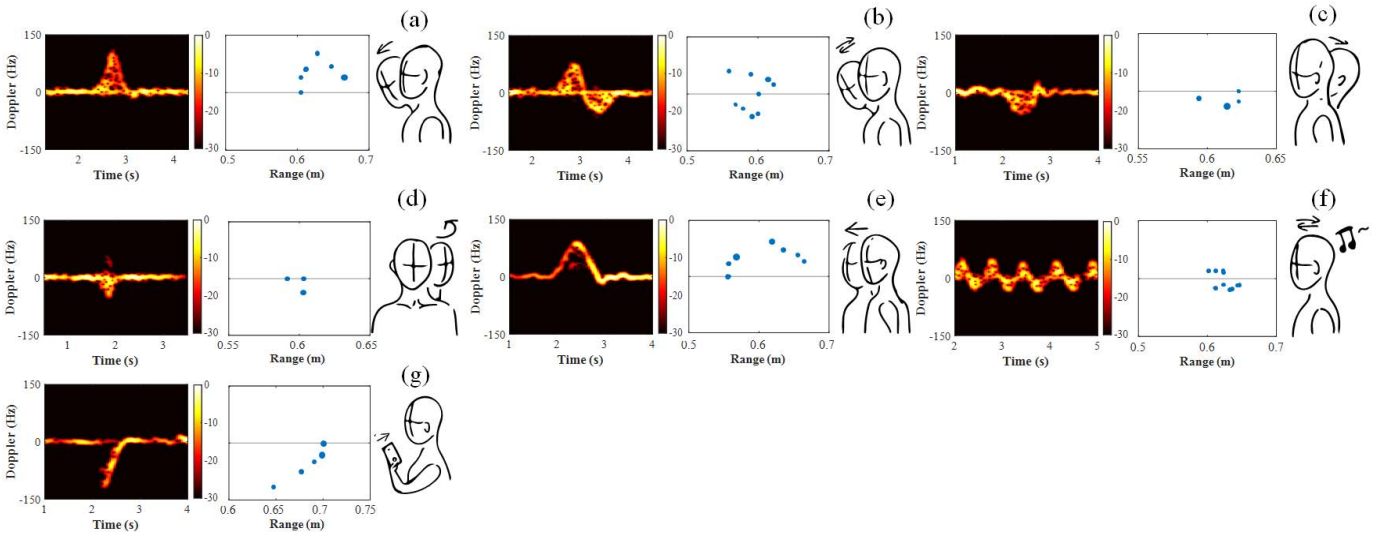

Fig. 8. Illustration of different driving behaviors and their corresponding time-Doppler spectrogram and range-Doppler trajectory based on the 24-GHz radar system in a moving car. (a)–(g) Seven typical driving behaviors related to inattentive driving.

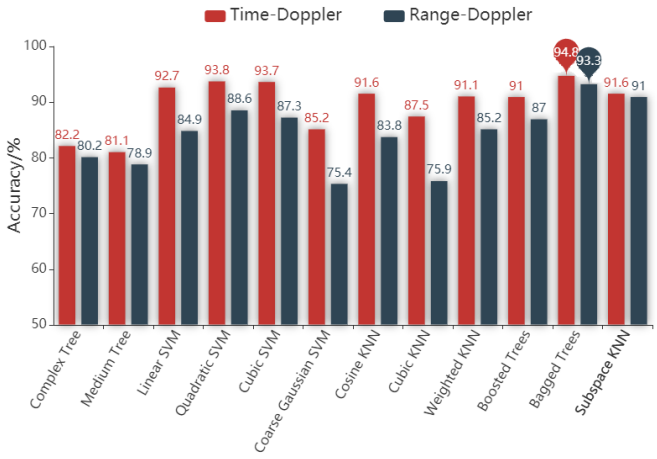

Fig. 9. Classification accuracies with different machine learning classifiers based on the time-Doppler spectrogram and range-Doppler trajectory.

TABLE VI
CONFUSION MATRIX OF CLASSIFICATION WITH TIME-DOPPLER SPECTROGRAM

Pred.[2] / Act.[1]	(a)[3]	(b)	(c)	(d)	(e)	(f)	(g)	TPR[4]
(a)	87	1			2			96.7%
(b)	1	88				1		97.8%
(c)			81	8			1	90%
(d)	1		5	84				93.3%
(e)	2				88			97.8%
(f)	2	3				84	1	93.3%
(g)			2	2		1	85	94.4%

[1] Act. means the actual samples.
[2] Pred. means the predicted samples.
[3] (a): Dorsal flexion; (b): Sleepy; (c) Dorsal hyperextension; (d) Rotation; (e) Forward body; (f) Shaking head; (g) Picking up a phone.
[4] TPR means true positive rate.

D. Classification Based on the Range-Doppler Trajectory

Based on the range-Doppler trajectory, an average accuracy rate of 93.3% was obtained. The detailed confusion matrix is shown in Table VII. Likewise, (a) dorsal flexion, (b) sleepy, and (e) forward body behaviors are the top three in recognition accuracy rate. On the other hand, (c) dorsal hyperextension obtained the lowest level of classification accuracy of 83.3%. Nine and six of them were misclassified as (d) rotation and (g) picking up a phone, respectively. Their similar trajectories in the range-Doppler domain make it difficult to distinguish them.

In addition, fusing features of both the time-Doppler spectrogram and the range-Doppler trajectory in classification was investigated. The recognition accuracy rate can be raised to 95.6%. However, the improvement may not be worth the increased computation load.

V. DISCUSSION

A. Individual Variability

The influence of individual diversity on the proposed method was also investigated. Indeed, detecting the driving behavior of unknown individuals based on trained data from known individuals would mirror the device's real-life application. For this purpose, five volunteers were randomly selected as the training group and the remaining volunteers as the test group. The data from the training group was used to train the machine learning classifier, and classification was performed using data from the test group. For each condition, each test was repeated 30 times to obtain a reliable evaluation. Fig. 10 shows test results as boxplots based on the time-Doppler spectrogram and the range-Doppler trajectory, respectively. The boxplot indicates the distribution of the test accuracy rates

TABLE VII

CONFUSION MATRIX OF CLASSIFICATION WITH RANGE-DOPPLER TRAJECTORY

Act. \ Pred.	(a)	(b)	(c)	(d)	(e)	(f)	(g)	TPR
(a)	87				3			96.7%
(b)		87			1	1	1	96.7%
(c)			75	9			6	83.3%
(d)	4		3	80		1	2	88.9%
(e)	2	1			87			96.7%
(f)				4		86		95.6%
(g)			2			2	86	95.6%

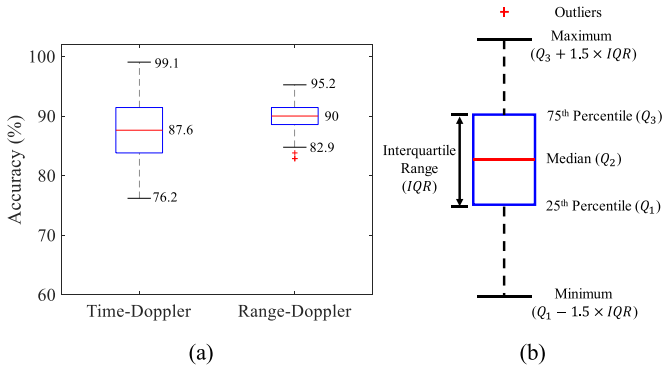

Fig. 10. Boxplots of recognition accuracies with the time-Doppler spectrogram and range-Doppler trajectory in individual diversity study. (a) Recognition accuracy in different conditions. (b) Legend of the boxplot.

in each condition. The upper and lower boundary of the blue box represents the third and first quartile of all the accuracy rates, which are denoted as Q_3 and Q_1, respectively. This means half of the test accuracy rates are located in the blue box. The size of the box, indicated by IQR, corresponds to its robustness. The red line in the box means the median value, which is denoted as Q_2. Points with values higher than $(Q_3 + 1.5 \times IQR)$ or lower than $(Q_1 - 1.5 \times IQR)$ are identified as outliers and marked by red crosses. As shown in Fig. 10, the results based on time-Doppler spectrogram could get a higher maximum and a lower minimum accuracy. In addition, there was a large gap between the upper and lower boundaries that signifies a considerable discrepancy among different individuals. On the other hand, the range-Doppler trajectory method showed a robust performance with a narrow blue box for unknown individuals.

B. Installation Position of the Radar System

The installation position of the radar system has a great impact and is worth studying experimentally. There are two straightforward options: one is to set the radar on the dashboard, and another is to set it on the rear-view mirror. The first position is exactly in front of the driver and can detect almost all the driver's behaviors. But the pitch angle of the radar needs to be adjusted according to the driver's sitting positions and postures. The other position can always directly point to the driver's head, bringing a perfect view angle for head tracking. However, as the rear-view mirror position is not placed on the central axis of the driver, body parts that are far away from the beam center may not be detected well. Furthermore, there is a possibility that careless drivers would not point the rear-view mirror correctly.

VI. CONCLUSION

This article proposed a novel method for inattentive driving behavior detection based on FMCW radar systems. Seven typical driving behaviors that may result in loss of attention were studied. Both time-Doppler spectrogram and range-Doppler trajectory were utilized to analyze their characteristics in multiple domains, including time, range, Doppler, and RCS. Experiments in a real car environment were conducted with six volunteers. Based on a Bagged Trees classifier, the recognition performance has been demonstrated with around 95% accuracy. Furthermore, the method based on the range-Doppler trajectory showed higher robustness than that of the time-Doppler spectrogram when facing individual diversity influences. Because range detection capability is highly desirable to focus the algorithm on the target of interest. The advantages and disadvantages of different radar installation positions were also discussed. In the future, more driving behaviors in a more complex road situation could be studied, and the database will be expanded. In addition, the feasibility of fusing multi-sensor information to achieve practical monitoring of driver status will be explored.

REFERENCES

[1] C. C. Liu, S. G. Hosking, and M. G. Lenné, "Predicting driver drowsiness using vehicle measures: Recent insights and future challenges," *J. Saf. Res.*, vol. 40, pp. 239–245, Aug. 2009.

[2] M. R. Ensley, "Toward a theory of situation awareness in dynamic systems," *Hum. Factors*, vol. 37, no. 1, pp. 85–104, Mar. 1995.

[3] G. Sikander and S. Anwar, "Driver fatigue detection systems: A review," *IEEE Trans. Intell. Transp. Syst.*, vol. 20, no. 6, pp. 2339–2352, Jun. 2019.

[4] A. Craig, Y. Tran, N. Wijesuriya, and H. T. Nguyen, "Regional brain wave activity changes associated with fatigue," *Psychophysiology*, vol. 49, no. 4, pp. 574–582, 2012.

[5] A. Craig, Y. Tran, N. Wijesuriya, and P. Boord, "A controlled investigation into the psychological determinants of fatigue," *Biol. Psychol.*, vol. 72, no. 1, pp. 78–87, Apr. 2006.

[6] S. Hu and G. Zheng, "Driver drowsiness detection with eyelid related parameters by support vector machine," *Expert Syst. Appl.*, vol. 36, no. 4, pp. 7651–7658, 2009.

[7] T. L. Morris and J. C. Miller, "Electrooculographic and performance indices of fatigue during simulated flight," *Biol. Psychol.*, vol. 42, no. 3, pp. 343–360, Feb. 1996.

[8] Y. Tran, N. Wijesuriya, M. Tarvainen, P. Karjalainen, and A. Craig, "The relationship between spectral changes in heart rate variability and fatigue," *J. Psychophysiol.*, vol. 23, no. 3, pp. 143–151, 2009.

[9] M. Patel, S. K. L. Lal, D. Kavanagh, and P. Rossiter, "Applying neural network analysis on heart rate variability data to assess driver fatigue," *Expert Syst. Appl.*, vol. 38, no. 6, pp. 7235–7242, 2011.

[10] S. K. Leem, F. Khan, and S. H. Cho, "Vital sign monitoring and mobile phone usage detection using IR-UWB radar for intended use in car crash prevention," *Sensors*, vol. 17, no. 6, p. 1240, 2017.

[11] Q. Zhang, Y. Zhou, S. Song, G. Liang, and H. Ni, "Heart rate extraction based on near-infrared camera: Towards driver state monitoring," *IEEE Access*, vol. 6, pp. 33076–33087, 2018.

[12] L. Ren, L. Kong, F. Foroughian, H. Wang, P. Theilmann, and A. E. Fathy, "Comparison study of noncontact vital signs detection using a Doppler stepped-frequency continuous-wave radar and camera-based imaging photoplethysmography," *IEEE Trans. Microw. Theory Techn.*, vol. 65, no. 9, pp. 3519–3529, Sep. 2017.
[13] T. Danisman, I. M. Bilasco, C. Djeraba, and N. Ihaddadene, "Drowsy driver detection system using eye blink patterns," in *Proc. Int. Conf. Mach. Web Intell.*, Algiers, Algeria, Oct. 2010, pp. 230–233.
[14] K. J. Raman *et al.*, "Fatigue monitoring based on yawning and head movement," in *Proc. 6th Int. Conf. Inf. Commun. Technol.*, May 2018, pp. 343–347.
[15] F. Vicente, Z. Huang, X. Xiong, F. D. L. Torre, W. Zhang, and D. Levi, "Driver gaze tracking and eyes off the road detection system," *IEEE Trans. Intell. Transp. Syst.*, vol. 16, no. 4, pp. 2014–2027, Aug. 2015.
[16] L. Ren *et al.*, "Short-time state-space method for micro-Doppler identification of walking subject using UWB impulse Doppler radar," *IEEE Trans. Microw. Theory Techn.*, vol. 66, no. 7, pp. 3521–3534, Jul. 2018.
[17] C. Gu and J. Lien, "A two-tone radar sensor for concurrent detection of absolute distance and relative movement for gesture sensing," *IEEE Sensors Lett.*, vol. 1, no. 3, Jun. 2017, Art. no. 3500504.
[18] Y. Li, Z. Peng, R. Pal, and C. Li, "Potential active shooter detection based on radar micro-Doppler and range-Doppler analysis using artificial neural network," *IEEE Sensors J.*, vol. 19, no. 3, pp. 1052–1063, Feb. 2019.
[19] F.-K. Wang, M.-C. Tang, Y.-C. Chiu, and T.-S. Horng, "Gesture sensing using retransmitted wireless communication signals based on Doppler radar technology," *IEEE Trans. Microw. Theory Techn.*, vol. 63, no. 12, pp. 4592–4602, Sep. 2015.
[20] C. Li *et al.*, "A review on recent progress of portable short-range noncontact microwave radar systems," *IEEE Trans. Microw. Theory Techn.*, vol. 65, no. 5, pp. 1692–1706, May 2017.
[21] T. Fan *et al.*, "Wireless hand gesture recognition based on continuous-wave Doppler radar sensors," *IEEE Trans. Microw. Theory Techn.*, vol. 64, no. 11, pp. 4012–4020, Nov. 2016.
[22] R. Chae, J. Wang, and C. Li, "FMCW radar driver head motion monitoring based on Doppler spectrogram and range-Doppler evolution," in *Proc. IEEE Top. Conf. Wireless Sensors Sensor Netw.*, Jan. 2019, pp. 1–4.
[23] C. M. Bishop, *Pattern Recognition and Machine Learning*. New York, NY, USA: Springer, 2006.
[24] K. Polat and S. Güneş, "Classification of epileptiform EEG using a hybrid system based on decision tree classifier and fast Fourier transform," *Appl. Math. Comput.*, vol. 187, no. 2, pp. 1017–1026, 2007.
[25] C.-C. Chang and C.-J. Lin, "LIBSVM: A library for support vector machines," *ACM Trans. Intell. Syst. Technol.*, vol. 2, no. 3, pp. 27:1–27:27, 2011.
[26] T. Chen, E. B. Mazomenos, K. Maharatna, S. Dasmahapatra, and M. Niranjan, "Design of a low-power on-body ECG classifier for remote cardiovascular monitoring systems," *IEEE J. Emerging Sel. Topics Circuits Syst.*, vol. 3, no. 1, pp. 75–85, Mar. 2013.
[27] Z. Zhou, *Ensemble Methods: Foundations and Algorithms*. London, U.K.: Chapman & Hall, 2012.
[28] L. Breiman, "Bagging predictors," *Mach. Learn.*, vol. 24, no. 2, pp. 123–140, 1996.
[29] Y. Freund and R. E. Schapire, "Experiments with a new boosting algorithm," in *Proc. 13th Int. Conf. Mach. Learn.*, Jul. 1996, pp. 148–156.
[30] T. K. Ho, "Nearest neighbors in random subspaces," in *Proc. Joint IAPR Int. Workshops Stat. Techn. Pattern Recognit. (SPR) Struct. Syntactic Pattern Recognit. (SSPR)*, 1998, pp. 640–648.
[31] R. Kohavi, "A study of cross-validation and bootstrap for accuracy estimation and model selection," in *Proc. 14th Int. Joint Conf. Artif. Intell.*, Aug. 1995, pp. 1137–1145.
[32] Z. Peng *et al.*, "A portable FMCW interferometry radar with programmable low-IF architecture for localization, ISAR imaging, and vital sign tracking," *IEEE Trans. Microw. Theory Techn.*, vol. 65, no. 4, pp. 1334–1344, Apr. 2017.
[33] Z. Peng, J. M. Muñoz-Ferreras, R. Gómez-García, L. Ran, and C. Li, "24-GHz biomedical radar on flexible substrate for ISAR imaging," in *Proc. IEEE MTT-S Int. Wireless Symp.*, Mar. 2016, pp. 1–4.
[34] G. Vinci *et al.*, "Six-port radar sensor for remote respiration rate and heartbeat vital-sign monitoring," *IEEE Trans. Microw. Theory Techn.*, vol. 61, no. 5, pp. 2093–2100, May 2013.

Chuanwei Ding (S'17) received the B.S. degree in electronic and information engineering from the Nanjing University of Science and Technology, Nanjing, China, in 2014, where he is currently pursuing the Ph.D. degree at the School of Electronic and Optical Engineering.

He is currently a Visiting Scholar with the Department of Electrical and Computer Engineering, Texas Tech University, Lubbock, TX, USA. His current research interests include biomedical applications of microwave technology and radar signal processing.

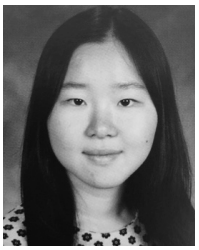

Rachel Chae (S'19) received the high school diploma from Woodbridge High School, Irvine, CA, USA, in 2019. She is currently pursuing the master's degree in biological engineering and electrical engineering at the Massachusetts Institute of Technology, Cambridge, MA, USA.

In the summer of 2018, she researched at the Department of Electrical and Computer Engineering, Texas Tech University, as a part of the Clark Scholars Program. Her current research interests include radar-based medical devices and biomedical imaging.

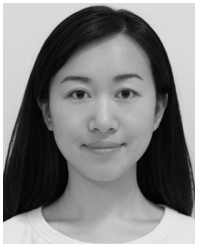

Jing Wang (S'17) received the B.S. degree in communication engineering from the Fujian University of Technology, Fuzhou, China, in 2015. She is currently pursuing the Ph.D. degree in electrical engineering at Texas Tech University, Lubbock, TX, USA.

Her current research interests include microwave circuits, wireless RF sensors, and their biomedical applications.

Li Zhang (S'17) received the B.S. degree from the Nanjing University of Science and Technology, Nanjing, China, in 2015, where he is currently pursuing the Ph.D. degree.

His current research interests include signal processing and machine learning technology in biomedical application.

Hong Hong (M'10) received the Ph.D. degree in electrical engineering from Nanjing University, Nanjing, China, in 2010.

In 2014, he was a Visiting Scholar with the Institute of Biomedical Engineering and Technology, The University of Sydney, Sydney, NSW, Australia. He is currently an Associate Professor with the School of Electronic and Optical Engineering, Nanjing University of Science and Technology, Nanjing. His current research interests include biomedical applications of microwave technology, audio signal processing, and radar signal processing.

Dr. Hong has been a Steering Committee member and a TPC member of the IEEE MTT-S International Microwave Biomedical Conference since 2018. He also serves as a member for the IEEE MTT-S Biological Effect and Medical Applications of RF and Microwave (MTT-10). He is a Guest Editor of the IEEE JOURNAL OF ELECTROMAGNETICS, RF AND MICROWAVES IN MEDICINE AND BIOLOGY.

Xiaohua Zhu (M'07) received the Ph.D. degree in communication and information system from the Nanjing University of Science and Technology, Nanjing, China, in 2002.

He is currently a Professor with the School of Electronic and Optical Engineering, Nanjing University of Science and Technology, Nanjing, and the Director of Radar and High-Speed Digital Signal Processing Laboratory, Nanjing University of Science and Technology, Nanjing. He has authored or coauthored 4 books and more than 100 articles. He has submitted 18 patent applications. His current research interests include radar system, radar signal theory, and digital signal processing.

Dr. Zhu was a recipient of the Ministerial and Provincial-Level Science and Technology Award (ten times).

Changzhi Li (S'06–M'09–SM'13) received the B.S. degree in electrical engineering from Zhejiang University, Hangzhou, China, in 2004, and the Ph.D. degree in electrical engineering from the University of Florida, Gainesville, FL, USA, in 2009.

From the summers of 2007 to 2009, he was with Alereon, Inc., Austin, TX, USA, and Coherent Logix, Inc., Austin, where he was involved in ultra-wideband (UWB) transceivers and software-defined radio, respectively. In 2009, he joined Texas Tech University, Lubbock, TX, USA, as an Assistant Professor, where he became an Associate Professor in 2014. His current research interests include biomedical applications of microwave technology, wireless sensors, and RF/analog circuits.

Dr. Li was a recipient of the IEEE Microwave Theory and Techniques Society (MTT-S) Outstanding Young Engineer Award, the IEEE Sensors Council Early Career Technical Achievement Award, the ASEE Frederick Emmons Terman Award, the IEEE-HKN Outstanding Young Professional Award, the NSF Faculty Early CAREER Award, and the IEEE MTT-S Graduate Fellowship Award. He served as a TPC Co-Chair for the IEEE Wireless and Microwave Technology Conference from 2012 to 2013 and the IEEE MTT-S International Microwave Biomedical Conference from 2018 to 2019. He served as an Associate Editor for the IEEE TRANSACTIONS ON CIRCUITS AND SYSTEMS–II: EXPRESS BRIEFS from 2014 to 2015. He is currently an Associate Editor of the IEEE TRANSACTIONS ON MICROWAVE THEORY AND TECHNIQUES, the IEEE TRANSACTIONS ON CIRCUITS AND SYSTEMS–I: REGULAR PAPERS, and the IEEE JOURNAL OF ELECTROMAGNETICS, RF AND MICROWAVES IN MEDICINE AND BIOLOGY.